Available online at www.sciencedirect.com
SCIENCE DIRECT®
Journal of Structural Biology 154 (2006) 168–183
Journal of Structural Biology
www.elsevier.com/locate/yjsbi

Estimation of variance in single-particle reconstruction using the bootstrap technique

Pawel A. Penczek [a,*], Chao Yang [b], Joachim Frank [c], Christian M.T. Spahn [d]

[a] The University of Texas–Houston Medical School, Department of Biochemistry and Molecular Biology, 6431 Fannin, MSB 6.218, Houston, TX 77030, USA
[b] Computational Research Division, Lawrence Berkeley National Laboratory, Berkeley, CA 94720, USA
[c] HHMI, Health Research, Inc., Wadsworth Center, Albany, NY 12201, USA
[d] Institut für Medizinische Physik und Biophysik, Universitätsklinikum Charité, Berlin, Germany

Received 24 October 2005; received in revised form 12 January 2006; accepted 17 January 2006
Available online 13 February 2006

Abstract

Density maps of a molecule obtained by single-particle reconstruction from thousands of molecule projections exhibit strong changes in local definition and reproducibility, as a consequence of conformational variability of the molecule and non-stoichiometry of ligand binding. These changes complicate the interpretation of density maps in terms of molecular structure. A three-dimensional (3-D) variance map provides an effective tool to assess the structural definition in each volume element. In this work, the different contributions to the 3-D variance in a single-particle reconstruction are discussed, and an effective method for the estimation of the 3-D variance map is proposed, using a bootstrap technique of sampling. Computations with test data confirm the viability, computational efficiency, and accuracy of the method under conditions encountered in practical circumstances.

Keywords: Single-particle reconstruction; Bootstrap; Electron microscopy

1. Introduction

Cryo-electron microscopy (EM), together with associated image processing techniques, has become an established method of structural analysis of large macromolecular complexes existing in single-particle form (i.e., as isolated particles) (Frank, 2006). It has become possible to reconstruct and visualize three-dimensional (3-D) density distributions of objects ranging from individual proteins (size 10–20 nm) (Ludtke et al., 2001), to protein–RNA complexes, such as ribosomes (size range 20–30 nm) (Gabashvili et al., 2000; Spahn et al., 2001), to highly symmetric structures of viruses (size range 30–150 nm) (Böttcher et al., 1997; Conway et al., 1997; Zhou et al., 2000). The technique is based on the assumption that the macromolecules are isolated, randomly oriented, and have identical structure. A suspension of molecules is placed on a grid, rapidly frozen, and transferred to the microscope. A single-exposure picture of a section of a grid is taken, yielding a micrograph filled with hundreds of projections of macromolecules frozen in various orientations. The distribution of orientations of particle views on the support grid depends on various factors and is in most cases non-uniform. Multiple micrographs are collected using various defocus settings of the microscope. After individual projections are selected from micrographs, their relative orientations in 3-D space are determined using alignment procedures (Penczek et al., 1992; Penczek et al., 1994; Penczek et al., 1996; van Heel et al., 2000) and the 3-D density distribution is calculated using a 3-D reconstruction algorithm (Harauz and van Heel, 1986; Marabini et al., 1998; Penczek et al., 1992; Radermacher, 1992). Although in terms of the best resolution achieved (0.7 nm for asymmetric molecules), single-particle cryo-EM cannot yet match

* Corresponding author. Fax: +1 713 500 0652.
E-mail address: Pawel.A.Penczek@uth.tmc.edu (P.A. Penczek).

1047-8477/$ - see front matter © 2006 Elsevier Inc. All rights reserved.
doi:10.1016/j.jsb.2006.01.003

X-ray crystallography, there are many advantages of this technique. Thanks to the rapid freezing of the specimen, molecules are captured in their native, aqueous environment, and their native structure is preserved. The electron microscope yields true projections of the Coulomb potential[1]; thus, in principle, an accurate representation of molecular densities can be obtained (Langmore and Smith, 1992). In addition, since the native form of the molecules is preserved, it is possible to study conformational changes and to examine dynamical effects of different functional states (Frank and Agrawal, 2000; Gao et al., 2003; Lata et al., 2000; Valle et al., 2003; Zhou et al., 2001).

The extent of the reproducibility of EM maps is reported in terms of ''resolution'', which is evaluated using one of the available methods, such as Fourier Ring/Shell Correlation (FRC/FSC) (Saxton and Baumeister, 1982), Differential Phase Residual (DPR) (Frank et al., 1981), or Spectral Signal-to-Noise-Ratio (SSNR) (Penczek, 2002a; Unser et al., 1987). These measures, constructed in Fourier space, are used to evaluate the self-consistency of Fourier information as a function of spatial frequency. The term ''resolution'', although often expressed in units of length, refers to the spatial frequency limit beyond which the information in Fourier space is dominated by noise (Penczek, 1998). In real space, this limit corresponds to a finite distance, (resolution distance), i.e., the minimum distance at which two point sources can be considered distinguishable. While the underlying analysis is performed in Fourier space and yields a non-uniform distribution of SSNR (and also Fourier space variance, see (Penczek, 2002a) for details), it only allows us to deduce the mean uniform distribution of the real-space error. To obtain a per-voxel distribution of errors, one would have to calculate the 3-D variance associated with the reconstructed object.

Although Fourier-space error measures in EM have been introduced over two decades ago, there has been relatively little effort devoted to evaluation of real-space errors. One could argue that for the analysis and interpretation of 3-D maps, the latter kind of evaluation is more important and certainly more useful. A straightforward way to assess the errors is to equate them with the standard deviation of the measured quantity, which can be derived through calculation of the variance. If available, knowledge of real-space errors in 3-D maps would be helpful in (i) detection of different functional states (for example, those characterized by binding of a ligand), (ii) analysis of conformational heterogeneity of the assemblies due to fluctuations of the structure around the ground state, (iii) analysis of the significance of small details in 3-D reconstructions, (iv) analysis of the significance of details in difference maps, (v) docking of known structural domains into EM density maps. For example, for both difference maps and for analysis of conformational variability, one should be able to verify that the difference between two maps being compared exceeds the standard deviation of the mass distribution by a reasonable margin. Similarly, the uniqueness and accuracy of docking can only be asserted if the error in the EM map is known (particularly if its distribution is non-uniform, as we can reasonably expect). Also, it is worth remembering that the underlying assumption in single-particle reconstruction is that the preparation is homogenous, i.e., the sample contains multiple replicas of the same macromolecule captured in the same conformational state. It is not clear to which extent this assumption is fulfilled in practice; there is mounting evidence that macromolecules occur naturally in a mixture of conformational states (Frank and Agrawal, 2000; Gao et al., 2004; Lata et al., 2000; Zhou et al., 2001). Moreover, macromolecular complexes are to a certain extent flexible and detection of such flexible regions can itself provide important biological information. An analysis of the phenomena described would be possible if the variance of the density distribution in real space could be evaluated.

Although the need for evaluation of 3-D variance in single-particle analysis has been recognized early, the problem proved to be quite challenging (Liu and Frank, 1995). The main difficulty is that the data are available in form of single projections, i.e., the information is partial. Thus, even if the variance of 2-D projection data is available, its relation to the variance in the reconstructed 3-D density map is not obvious. In addition, in single-particle reconstruction the particle images (projections) originate from different 3-D structures. If these structures fall into different classes, due to conformational changes or non-stoichiometry of ligand binding, the obvious course of action would be to reconstruct 3-D structures from subsets of projections corresponding to the respective classes and calculate the 3-D variances directly using the resulting volumes. Unfortunately, this is not possible as we do not know the class membership of single projections. In other words, we have to recognize that *there is only one data set* of projection, while for the calculation of the variance we would have to know *which particle view corresponds to which class of macromolecules*. Finally, we have to keep in mind that the exact inversion of the projection process is impossible. Thus, the process of 3-D reconstruction itself is a source of errors.

The problem of estimating the variance in images reconstructed from sets of their projections attracted significant attention in the field of Positron Emission Tomography (PET) (Leahy and Qi, 2000). For linear reconstruction methods, it is easy to derive an analytical expression for the variance (Barrett, 1990). Due to popularity of the linear Filtered Backprojection (FBP) reconstruction algorithm in PET applications, its variance properties have been studied extensively (Carson et al., 1993; Maitra, 1997; Maitra and O'Sullivan, 1998; Palmer et al., 1985). It was demonstrated that for FBP, given estimates of the variance in projections and assuming the independence of the underlying sources of noise, the variance in the reconstructed image, including

[1] The limitations due to the curvature of Ewald's sphere can be ignored for the combination of object size, microscope voltage, and achievable resolution in single-particle reconstruction.

contributions from the FBP algorithm itself, can be calculated relatively easily and efficiently using the FFT technique (Maitra, 1997). Subsequently, attention shifted to explorations of variance properties of maximum likelihood (ML) and maximum a posteriori (MAP) image reconstruction methods. These methods can combine physical models of image formation in PET and the statistical nature of the data (Poisson distribution) with an inclusion of priors enforcing smoothness of the reconstructed image; therefore, MAP and ML reconstruction algorithms are widely used in PET applications. Unfortunately, since ML and MAP are non-linear and iterative, explicit formulae of the reconstruction variance for these algorithms are not available. Nevertheless, a number of ML and MAP analytical methods for resolution and variance estimation have been proposed based on simplifying assumptions (Barrett et al., 1994; Fessler, 1996; Fessler and Rogers, 1996; Qi and Leahy, 1999, 2000; Wilson and Tsui, 1993). To free the analysis of statistical properties of PET images from the dependence on the reconstruction algorithm used and from the assumption of the Poisson noise in projections, the use of resampling techniques was suggested (Haynor and Woods, 1989), particularly the bootstrap (Buvat, 2002; Dahlbom, 2002; Maitra, 1998). Resampling techniques are computationally intensive, but they yield excellent results irrespective of the complexities of the reconstruction process.

Despite the development of comprehensive error analysis methods for PET applications, very few of these methods can be directly used in the context of cryo-EM. Although FBP is used in single-particle reconstruction, it is implemented in a generalized form that accounts for uneven distribution of projections in EM (Radermacher, 1992). In recent years, other reconstruction algorithms were introduced and increasingly used in cryo-EM (Lanzavecchia et al., 1999, 2002; Marabini et al., 1998; Penczek et al., 1992), particularly those employing direct Fourier inversion of the 3-D ray transform (Grigorieff, 1998; Penczek et al., 2004). It is not clear whether analytical formulae for variance could be derived for all these algorithms. Bootstrap methods developed for PET take advantage of its particular mode of data collection and cannot be directly transferred to cryo-EM image collection paradigm. Finally, as we will argue later, single-particle reconstruction has its own set of requirements and constraints that have to be addressed if the analysis of variance is to yield practical results.

It is curious that estimation of real-space variance in single-particle reconstruction has attracted little attention. Despite the fact that the interpretation of 3-D maps is often performed at the limit of their resolution, little is known about the distribution of error in real space. A method for estimation of variance of a 3-D map reconstructed from projections by a general weighted backprojection (GWBP) algorithm was proposed in (Liu and Frank, 1995). The authors start by introducing two "types" of the variance: (i) type I, associated with the estimate of the variance in projection data, and (ii) type II, which could be calculated only if we could collect entire set of projections for each macromolecule so it could be reconstructed unambiguously. In this formulation, the type-II variance would be calculated according to the definition of variance, using multiple available reconstructions, and could be employed to study conformational variability of macromolecules. The authors of that study recognized that unless one can assign projections to classes that correspond to homogenous sets of macromolecules, the calculation of the type-II variance of reconstructed objects might be impossible. Similar conclusions were drawn in (Ushakov and Ushakova, 1998). To calculate the type-I variance, the authors introduced two possible methods of variance estimation in the projection data: (i) one that takes advantage of the availability of multiple projection images assigned to a given projection direction, (ii) a second one, in which the variance is estimated by comparison of projection data with reprojections of the reconstruction. The type-I variance is then calculated using GWBP algorithm by backprojecting the weighted and filtered projection variances. In general, the derivation of the method is based on rather restrictive assumptions, i.e., that the noise in projections is independent. This limits its usefulness for cryo-EM applications, particularly if conformation changes of macromolecule and the influence of the contrast transfer function (CTF) of the microscope are to be considered. In (Haley et al., 1998) it was suggested that a 3-D variance map can be calculated by backprojecting the modulus of the differences between projection data and re-projections of the structure, and the method was attributed to M. van Heel. Effectively, this is the same approach as espoused by Liu and Frank (Liu and Frank, 1995).

In this study, we will demonstrate that a meaningful estimate of the real-space variance (corresponding to type-II variance of Liu and Frank), including the variance caused by the reconstruction algorithm itself, can be calculated taking advantage of the availability of a large number of 2-D projections and by using a bootstrap technique. More importantly, the covariance of the 3-D reconstructed volume can also be calculated, making the analysis of conformational variability of macromolecules possible.

The article is organized as follows. In Section 2, we introduce the basic notation and provide an expression for the variance following a linear reconstruction method. In Section 3, we discuss various sources of errors in 3-D reconstructions from projections in single-particle reconstruction. We proceed with a discussion of the concept of the variance of a 3-D reconstruction and postulate that there are three different categories of such a variance. In Section 4, we introduce the bootstrap method and describe its efficient implementation using a variant of a 3-D reconstruction method employing direct Fourier inversion. In Section 5, we provide test results for the introduced variance estimation algorithm introduced. For the bootstrap method, we analyze the consistency and the error of the variance estimate using Monte-Carlo simulations as a function of the number of bootstrap volumes calculated. This

provides a practical way of deciding how many bootstrap volumes have to be calculated to obtain the desired accuracy of the variance estimate. We proceed with tests of the bootstrap method using simulated data for various models of the variance in single-particle reconstruction and demonstrate that it yields acceptable results. We demonstrate that the expectation maximization algorithm (described in the Supplementary Material) yields erroneous results in the case of correlated noise in the structure. We also demonstrate that using the bootstrap method we can estimate the covariance (i.e., intervoxel correlations) within the reconstructed 3-D density map. Additional test results of the bootstrap method are provided in the Supplementary Material. In the closing Section 6 we point out the conceptual difficulties caused by the presence of alignment errors in the projection data and we discuss practical ways to account for the effects of the transfer function of the microscope.

The results of the application of the bootstrap method to the analysis of the 70S *Escherichia coli* ribosome complexed with EF-G and tRNAs are described in a companion paper by Penczek et al.

2. Notation

In the weak-phase approximation (Wade, 1992), a 2-D image g collected in the electron microscope is a parallel beam projection P (ray transform) of the 3-D Coulomb potential distribution of a macromolecule f. The projection in the direction of the z axis is

$$g_z(x,y) = \int f(x,y,z)\mathrm{d}z. \tag{1}$$

This integral transformation is continuous, linear, and shift-invariant. We will write the full ray transform as

$$g = Pf. \tag{2}$$

We assume that an inverse transformation $P^{\dagger}$ exists and that it is regularized by a 'smoothing' operator S

$$\hat{f} = SP^{\dagger}g, \tag{3}$$

where $\hat{f}$ is an approximate reconstruction of f from projection data g.

In the discrete case, $\mathbf{f}$ is a vector containing n arbitrarily arranged voxels of the 3-D structure, $\mathbf{g}$ is a vector containing correspondingly arranged m pixels of k 2-D projections, and $\mathbf{P}$ is an $m \times n$ matrix with entries p_{ij} whose values depend on the interpolation scheme used and on the projection directions. For the often used trilinear interpolation, the relationship $0 \leqslant p_{ij} \leqslant 1$ holds. In addition, in single-particle reconstruction, $m \gg n$ and matrix $\mathbf{P}$ is sparse with $O(\sqrt[3]{n})$ non-zero entries per row. Thus, in the discrete representation, pixels in projections are linear combinations of corresponding voxels of the 3-D structure

$$g_i = \sum_{j=1}^{n} p_{ij} f_j, \quad i = 1, \ldots, m. \tag{4}$$

By $\mathbf{P}^{\dagger}$ we denote any linear and shift-invariant reconstruction algorithm, for example a least-square pseudo-inverse solution

$$\hat{\mathbf{f}} = \mathbf{S}\left(\mathbf{P}^{\mathrm{T}}\mathbf{P}\right)^{-1}\mathbf{P}^{\mathrm{T}}\mathbf{g} = \mathbf{S}\mathbf{P}^{\dagger}\mathbf{g} = \mathbf{R}\mathbf{g}, \tag{5}$$

where $\mathbf{S}$ is a matrix representation of the appropriate low-pass filter and $\mathbf{P}^{\dagger}$ is an $n \times m$ "reconstruction matrix". $\mathbf{R}$ denotes any linear reconstruction algorithm, for example GWBP, direct Fourier inversion, or algebraic iterative reconstruction (SIRT).

The variance of a random vector $\mathbf{f}$ is given by

$$\sigma_{\mathbf{f}}^2 = \left\langle \mathbf{f}^2 \right\rangle - \langle \mathbf{f} \rangle^2, \tag{6}$$

where $\langle\rangle$ denotes the expectation value and $\sigma_{\mathbf{f}}^2$ is a vector containing variances of components of the vector $\mathbf{f}$ as its elements, and squaring of the vector is understood componentwise. The standard deviation $\sigma_{\mathbf{f}}$ will be associated with the error of vector $\mathbf{f}$. Finally, the covariance of $\mathbf{f}$ is

$$\mathbf{C}_{\mathbf{f}} = \left\langle (\mathbf{f} - \langle \mathbf{f} \rangle)(\mathbf{f} - \langle \mathbf{f} \rangle)^{\mathrm{T}} \right\rangle = \left\langle \mathbf{f}\mathbf{f}^{\mathrm{T}} \right\rangle - \langle \mathbf{f} \rangle \langle \mathbf{f} \rangle^{\mathrm{T}}. \tag{7}$$

By combining Eq. (5) with Eq. (7), we obtain an expression for the covariance matrix of the reconstruction $\hat{\mathbf{f}}$

$$\mathbf{C}_{\hat{\mathbf{f}}} = \mathbf{R}^{\mathrm{T}}\mathbf{C}_{\mathbf{g}}\mathbf{R}, \tag{8}$$

where $\mathbf{C}_{\mathbf{g}}$ is the covariance matrix of the projection data $\mathbf{g}$.

3. Sources of variance in EM single-particle structure determination

3.1. Sources of variability

The process of image formation in electron microscopy is well understood (Wade, 1992). In the weak-phase approximation, image formation can be approximated by a linear model according to which the observed projections of ice-embedded macromolecules are linearly related to the molecules' Coulomb potential with additional modification by a (linear) transfer function. The image contrast is formed as a result of the interaction of the electrons with the specimen and the data are collected either on film, subsequently digitized, or directly in digital form in the microscope using a CCD camera. Usually, the microscope is operated with an accelerating voltage in the range of 100–300 kV. To minimize radiation damage, the pictures are taken under low-dose conditions and the dose is kept at $\sim$10 $e^-/Å^2$. With a typical pixel size ranging from 2×2 to 5×5 $Å^2$, the average number of electron counts per pixel is sufficient to justify a Gaussian approximation of their distribution.

We can identify six major sources of noise in electron microscopy:

(1) *The specimen*: (i) impurities in the sample, such as the presence of minor contaminants, for example extra protein; (ii) induced disorder caused by the preparation and imaging procedures, for example, from

radiation damage, dehydration effects, or stain-induced effects (i.e., variability and granularity of stains); (iii) inherent disorder or irregularities at the atomic, molecular, or macromolecular level, in particular conformational variability of the macromolecules; and (iv) non-stoichiometry of ligand binding.

(2) *Medium surrounding the specimen*: in cryo-EM it is amorphous ice.

(3) *Specimen support film*: preparation and imaging of many proteins is facilitated by addition of a thin layer of supporting carbon film, which introduces "structural noise."

(4) *The microscope*: thermal drift, mechanical vibrations, electrostatic charging, the electron statistics, and electron scattering events unrelated to the specimen.

(5) *Data collection*: when the data is collected on film, its granularity will be a source of noise; subsequent analog-to-digital conversion will introduce digitization noise that depends mainly on the dynamical range of the data relative to the number of bits in the converter; CCD cameras, in addition to digitization noise, contribute scintillator noise and noise introduced by the readout amplifier.

(6) *Image processing*: single-particle images are represented in discrete form as 2-D arrays of floating point numbers. In the course of establishing the geometrical relations between the images (alignment) and calculation of the 3-D map (3-D reconstruction), they have to be shifted by non-integer pixel values and rotated both in 2-D and in 3-D. These steps involve interpolations required to approximate image values between grid points. Interpolation will result in loss of high-frequency information and injection of spurious information. Finally, misalignment of particle images should be considered a major source of noise.

Despite the large number of sources of noise, our measurements (2-D images) basically contain two regions with distinct statistical properties: the background and the particles. The former can be considered a sample of the noise of the data collection process, while the latter contains a superposition of the signal with two kinds of noise: the background noise and the noise due to the variability of the specimen (Penczek, 2002b). In addition, some of the sources listed contribute noise that is uncorrelated between pixels in projections (for example, the noise due to granularity of the film), while others contribute correlated noise (any source affected by the CTF of the microscope will generate noise that is necessarily correlated). Note that subsequent image processing steps, prior to or during the step of 3-D reconstruction, will introduce additional correlations between pixels.

In the present work we will ignore any effects due to the CTF. This facilitates the analysis and significantly simplifies the design of the variance estimation methods, at the acceptable cost of limiting the resolution of the variance maps thus obtained.

3.2. Categories of variance

For the purpose of the current analysis, we will group the sources of noise listed according to their contributions to the noise in the 3-D map and according to our ability to recover the distribution of this noise upon the process of 3-D reconstruction from projections. We will introduce three main categories of variance and, for the purpose of easier identification, we will term them based on the broad understanding of their respective sources (see also Table 3):

1. *Solvent variance* σ^2_{Solv}: the solvent variance relates exclusively to the imaged specimen and the surrounding solvent, not to the reconstructed object. The main sources of this variance are: (i) irregularities of the medium (ice) surrounding the particle and (ii) the variation of the macromolecules that is due to radiation or thermal instabilities. These two sources are affected by the CTF. Additional components of the solvent variance are those that are conceptually different, but which cannot be distinguished from the two main components; i.e., the variance due to support film, the microscope, the data collection process, and some of the steps of image processing. Some of these sources are not affected by the CTF. If the CTF is ignored, all sources of the noise listed can be considered uncorrelated, although their spatial distribution can be non-uniform. For example, if the distribution of mass density of the macromolecule is $f(x, y, x)$, the associated variance can have the form of $\sigma^2_{\mathrm{Solv}}(f(x, y, x))$, i.e., it is a function of the spatially varied mass density. The information about the solvent variance can be used to estimate the distribution of noise in the imaged specimen and also, to some extent, the degree of noise uniformity.
2. *Structure variance* σ^2_{SVar}: the variance in the reconstructed 3-D map is due to five possible sources: (i) reconstruction algorithm and non-uniform distribution of projections, (ii) background noise, (iii) misalignment errors, (iv) conformational variability of the macromolecule, and (v) presence or absence of a ligand. Sources (iii–v) have long-range correlations; moreover, we expect that variations in different regions of the reconstructed structure will tend to be correlated (for example, binding of ligand can cause conformational changes in distant regions of the protein). For the purpose of easier identification, we will use the following terms for two components of the structure variance:

   2a. *Reconstruction variance* σ^2_{Rec}: the variance in the 3-D map that is due to the reconstruction algorithm and the uneven distribution of projection directions. The inversion of the ray transform is an ill-posed problem and even in the absence of noise, the reconstruction process will introduce artifacts in the structure, particularly if we consider that the distribution of projection directions varies between experiments. The level and distribution of the reconstruction variance informs us about the stability of the

reconstruction algorithm under practical image collection conditions.

2b. *Background variance* σ^2_{Back}: the variance in the reconstructed 3-D map that is not due to the structure. Sources of this variance include any noise in projection data, particularly those contributions listed under solvent variance. The background variance is the variance of the noise modified by the reconstruction process, i.e., it is modified by the associated filtration and averaging in Fourier space. We will assume that the background variance is well represented by the distribution of noise in the micrograph background and that the noise within the particle area has essentially the same distribution. By extension, we will assume that the resulting background variance in 3-D reconstruction is uniform (or nearly so). The information on the background variance can be used for the purpose of evaluation of docking accuracy. It also provides a reference level of error, i.e., information about the minimum possibly achievable level of noise in the reconstructed object if there were no alignment errors and the particles were truly homogenous.

3. *Variance of structures* σ^2_{Struct}: the variance due to conformational variability or non-stoichiometry of ligand binding, which could be calculated if, for each macromolecule, we had an entire set of projections, sufficient to reconstruct it unambiguously. This variance is closely related to, and derived from, the structure variance, but it differs from the latter in the exclusion of the background noise and in numerical aspects. In distinction from the structure variance, which corresponds to the variance associated with averages of mixtures of different structures, the *variance of structures* corresponds to the variance of unique structures; thus, its numerical value can be expected to be much higher (Fig. 1). Knowledge of the variance of structure can be used to guide docking experiments; it can also indicate presence of alignment errors, heterogeneity of the sample, or the location of ligands. Note that the variance of structures is not directly accessible in single-particle reconstruction, as projections originate from different macromolecules, and each projection carries only partial information about the 3-D structure.

In the nomenclature introduced by Liu and Frank (Liu and Frank, 1995), the solvent variance is of type I, while the variance of structures is of type II.

The three categories of variance listed above share the following two major distinctions: (i) whether or not the sources of errors are correlated and (ii) whether we consider the variance of the *imaged object* (or background) or the variance of the *reconstructed object* (or background). We will demonstrate that each of these categories calls for a different computational approach and each will result in quite different estimates of noise. Nevertheless, each carries important information about the statistics of the experiment, and each can therefore be used for different purposes in the variance estimation.

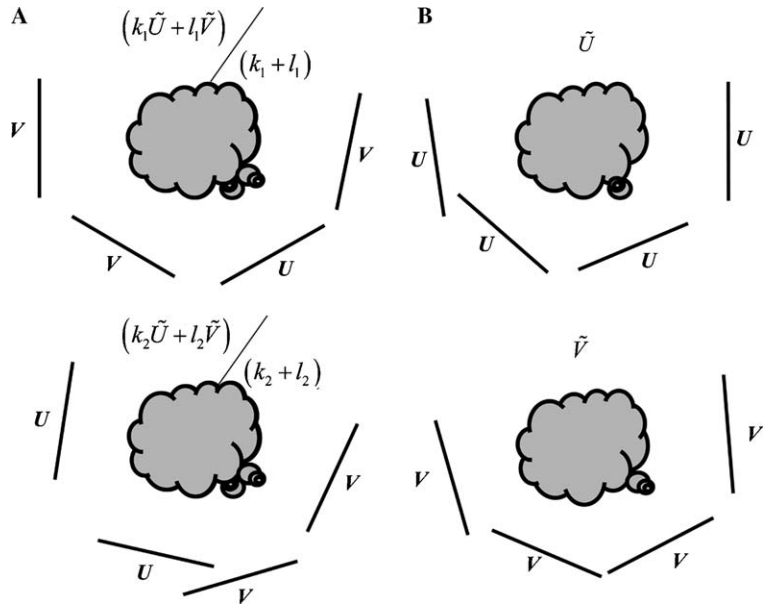

Fig. 1. Structure variance versus variance of structures in case of two conformers $\tilde{U}$ and $\tilde{V}$ of a macromolecule. (A) In single-particle reconstruction, a data set contains projections U and V of two conformers mixed in unknown quantities k and l, respectively. Repeated experiment would yield projection data in different quantities and at different angular directions. The variance calculated in this case will yield the structure variance, i.e., the variance corresponding to variability of different "average" reconstructions. (B) If the assignments of projections were available, each conformer could be reconstructed unambiguously. This would yield the variance of structures, i.e., the variance of reconstructed actual conformers. Since the assignment of projections is not known, this variance is not directly accessible in single-particle reconstruction.

4. Application of the bootstrap technique to the variance estimation

In Section 2, we showed that to calculate variance/covariance $\mathbf{C}_{\hat{\mathbf{f}}}$ of the 3-D reconstruction $\hat{\mathbf{f}}$ we would have to estimate variance/covariance $\mathbf{C}_{\mathbf{g}}$ of the projection data $\mathbf{g}$ (Eq. (8)). This is impractical because of the very large size of the matrix $\mathbf{C}_{\mathbf{g}}$ and because we do not have an efficient algorithm for calculating $\mathbf{C}_{\hat{\mathbf{f}}}$ from $\mathbf{C}_{\mathbf{g}}$.

In addition to the calculation of the variance of the reconstruction we would like to calculate the variance of the reconstructed structure. The two are not the same, as can be deduced by the following reasoning. In single-particle reconstruction, each projection image originates from a different macromolecule. If macromolecules were identical and there was no alignment error, the only source of errors in the reconstruction would be the additive noise in the projections and the reconstruction algorithm itself. In reality, macromolecules do vary in structure. Thus, if we could collect a number of projections sufficient for calculating the 3-D reconstruction of every macromolecule, Eq. (5) could be written as:

$$\hat{\mathbf{f}} = \mathbf{R}(\mathbf{g}_1 + \mathbf{g}_2 + \mathbf{g}_3 + \ldots), \tag{9}$$

where $\mathbf{g}_k$ denotes a set of projections associated with the *k-th* structure. If we could sort projections into these k homogenous sets, we could calculate 3-D reconstructions $\hat{\mathbf{f}}_k = \mathbf{R}\mathbf{g}_k$ and—from the definition – their variance $\sigma^2_{\hat{\mathbf{f}}}$. This variance we will call the *variance of structures* (recall it is the Type-II variance of Liu and Frank (Liu and Frank, 1995)). In practice we do not know which projection originated from which structure, so we can only divide the set of projection randomly into subsets and calculate the corresponding 3-D reconstructions. Since each subset contains projections from different structures, the *structure variance* σ^2_{SVar} of reconstructions thus obtained will be necessarily smaller than the "true" variance of the original, albeit unknown structures, and also smaller than the variance of structures, i.e., $\sigma^2_{\mathrm{SVar}} < \sigma^2_{\mathrm{Struct}}$. The two could be equal only if all macromolecules were identical and if there were no alignment errors. It is important to note that in each case the portion of variance in reconstructions that is due to uncorrelated noise in projections is the same; clearly, since the noise is uncorrelated, its contribution cannot be reduced by exchanging projections between different groups. Also, since we only consider molecules reconstructed from projections, both variances contain contribution from the variance due to the reconstruction algorithm.

In this section we will demonstrate that the variance/covariance of a 3-D reconstruction can be calculated relatively efficiently using the bootstrap technique. Moreover, we will also show that the variance of structures is related to the structure variance in a simple manner, and that its magnitude can be estimated if the level of background variance is known.

4.1. The bootstrap technique for the estimation of the variance in a 3-D structure calculated from a set of its projections

To estimate the variance/covariance in a structure calculated from the set of its projections in our earlier work (Penczek, 2002b) we proposed to employ a statistical resampling technique, the bootstrap (Davison and Hinkley, 1997). This method is particularly useful for the estimation of parameters of statistical distributions when analytical formulae are not known. The idea is to resample the original data set to create replicate sets, from which quantities of interest can be calculated. Bootstrap is based on resampling with replacements, and in our application we propose to resample the available set of K projections, as was put forward in (Penczek, 2002b).

The voxels in the reconstructed volume can be considered to be (weighted) sums of pixels in projections. If we assume that the number of 2-D projections is large and the weighting function of the reconstruction algorithm does not change much by removing or adding a subset of projections, then we propose to calculate the variance of structures $\sigma^2_{\mathrm{Struct}}$ by using a relationship between the variance of arithmetic means for sampling with replacements and the sample variance (Hansen et al., 1953)

$$\sigma^2_{\mathrm{Struct}} = K\sigma^2_B. \tag{10}$$

In what follows, we will demonstrate that the above relationship holds only for components of the variance that are related to the structure, not for the components due to uncorrelated noise, and we will show that σ^2_B is the structure variance σ^2_{SVar}.

In the bootstrap procedure, a new set of projections is generated by randomly selecting, with replacements, projections from the original set. Thus, in the new set some of the projections will be omitted and some will be represented more than once. Using this set, a 3-D sample structure is calculated. This process is repeated B times. The resulting B bootstrap volumes are low-passed filtered to a resolution not exceeding the resolution of the analyzed structure, and the voxel-by-voxel bootstrap variances σ^2_B as well as covariances between voxels (or regions within the structure) are calculated. The covariance or, taking advantage of the fact that both variance and covariance of the mean are related to those of the sample by the same factor K, the corresponding cross-correlation coefficient can be estimated by

$$r_{ij} = \frac{\frac{1}{B}\sum_{l=1}^{B}\left(v_i^l - \bar{v}_i\right)\left(v_j^l - \bar{v}_j\right)}{\sigma_{B_i}\sigma_{B_j}}, \tag{11}$$

where i and j are indices of two different voxels/regions in a 3-D bootstrap structure, and v_i^l and $\bar{v}_i$ are the values of the i'-th voxels/regions for the l'-th structure and its average, respectively.

Application of the bootstrap technique to the variance estimation in 3-D reconstruction has the major advantage that it does not depend on the choice of a particular 3-D

reconstruction algorithm; rather, the approach is general, i.e., applicable to any reconstruction algorithm as long as it is linear. This freedom of choice is important not only because the quality of reconstruction algorithms varies but, more importantly, because of considerations of computational efficiency. Since bootstrap reconstructions can be generated from an overall reconstruction simply by removing certain projections and increasing the multiplicity of others, we should employ a 3-D reconstruction in which such modifications can be performed in an efficient way. A possible approach is to use a straightforward direct Fourier inversion scheme based on the projection theorem for the 3-D ray transform, which states that the 2-D Fourier transform of a projection of a 3-D object equals the 3-D Fourier transform of this object on a central plane perpendicular to the projection direction. Thus, one can compute 2-D Fourier transforms of the available projections and add Fourier pixels to voxels of the target 3-D Fourier transform using a simple nearest-neighbor (NN) interpolation scheme (Penczek, 2002a). Before the 3-D Fourier inversion, the accumulated Fourier coefficients have to be divided by the respective numbers of added Fourier pixels (the weighting functions). Incidentally, the accuracy of this reconstruction scheme can be greatly improved if the projections are padded with zeroes in real space to increase their size fourfold (N. Grigorieff, personal communication). The padding results in a finer Fourier grid and thus reduces the nearest-neighbor interpolation errors.

The Bootstrap method for 3-D variance estimation using direct Fourier inversion with NN-interpolation:

(i) pad K projection images with zeroes fourfold;
(ii) calculate and store FFTs of padded projections;
(iii) compute and store 3-D Fourier volume using NN-interpolation.

for $\ell = 1, 2, \ldots, B$

(a) using selection with replacements, generate K bootstrap projection indices $(i_1, i_2, \ldots, i_K)_\ell$;
(b) based on the set of projection indices $(i_1, i_2, \ldots, i_K)_\ell$, either remove or add projections to the pre-computed 3-D Fourier volume;
(c) compute inverse 3-D inverse FFT of the Fourier volume and extract the part containing the structure. This yields bootstrap volume V_ℓ.

end for

Compute 3-D bootstrap variance map:

$$\sigma_B^2 = \frac{1}{B-1}\sum_{\ell=1}^{B}\left(V_\ell - \frac{1}{B}\sum_{j=1}^{B} V_j\right)^2.$$

The approach adopted results in a particularly straightforward and efficient implementation of the bootstrap technique. In addition, due to the nature of the method, the bootstrap reconstructions can be generated entirely independently in parallel, using either the shared or distributed memory paradigm. For example, the data set described in the companion paper on the application of the bootstrap method contained 10,477 2-D particle images boxed in windows of 75×75 pixels. Using a shared memory (OpenMP) implementation we were able to generate 90 bootstrap volumes using 1 wall clock hour of SGI 3200 ORIGIN equipped with 8×400 MHz processors and 8 GB main memory.

4.2. Application of the bootstrap method to the variance estimation in a general case

In a general case, the variance in the 3-D reconstruction, which we call *the structure variance*, will contain the variance due to the reconstruction algorithm and distribution of projections σ^2_{Rec}, due to background noise in projections σ^2_{Back}, due to alignment errors σ^2_{Ali}, and due to conformational variability of the 3-D structure σ^2_{Conf} (for example due to structural variability or non-stoichiometric binding of ligands). This compound variance can be equated to the bootstrap variance and calculated using the bootstrap technique

$$\sigma^2_{\mathrm{SVar}} = \sigma^2_B = \sigma^2_{\mathrm{Conf}} + \sigma^2_{\mathrm{Ali}} + \sigma^2_{\mathrm{Rec}} + \sigma^2_{\mathrm{Back}}. \quad (12)$$

In a series of tests described in the Supplementary Material we demonstrated that the bootstrap technique yields very good estimates of three of the components of the right hand side of Eq. (12), namely σ^2_{Ali}, σ^2_{Rec}, and σ^2_{Back}. However, if we wish to calculate the variance of structures $\sigma^2_{\mathrm{Struct}}$ using Eq. (10), we have to eliminate from σ^2_B all those components that would remain the same if we were able to calculate the variance of structures directly, i.e., by collecting an entire set of projections and calculating an independent reconstruction for each macromolecule (Eq. (9)). Clearly, the components included in Eq. (12) that fall into this category are σ^2_{Ali}, σ^2_{Rec}, and σ^2_{Back} and they have to be calculated independently. Thus, the variance of structures should be calculated using an appropriately modified version of Eq. (10), that is:

$$\sigma^2_{\mathrm{Struct}} = K\left(\sigma^2_B - \sigma^2_{\mathrm{Ali}} - \sigma^2_{\mathrm{Rec}} - \sigma^2_{\mathrm{Back}}\right). \quad (13)$$

A major difficulty is caused by the misalignment variance σ^2_{Ali}. Although, as shown in the Supplementary Material, in the absence of other components, σ^2_{Ali} can be accurately estimated using the bootstrap technique, it cannot be distinguished from the variance due to conformational variability of 3-D structure σ^2_{Conf}. In other words, σ^2_{Ali} has the same statistical properties as σ^2_{Conf}, but while the latter has to be multiplied by the number of projections K to yield the correct level of the variance of structures $\sigma^2_{\mathrm{Struct}}$ using Eq. (10), the former should not. Unfortunately it is not immediately apparent how one could design a method that would allow us to distinguish between the two components (Baldwin and Penczek, 2005).

4.3. Calculation of the background variance

If we assume that the statistical distribution of noise in micrographs is known, it should be possible, in principle, to derive from it the statistical distribution of noise in the reconstruction. For example, if the projection directions were distributed uniformly, the distribution of noise in the reconstructed volume would be modified by a filter $h(\omega) = \sqrt{\omega_x^2 + \omega_y^2 + \omega_z^2}$, where ω is the spatial frequency. This filter reflects the degree of oversampling in the reconstruction. For some 3-D distributions of projections (uniform, single-axis tilt), the appropriate filter can be calculated analytically and the resulting modification of the power spectrum of the noise can also be calculated. Unfortunately, this is not the case in single-particle reconstruction, where the distribution of projections is random and non-uniform. Therefore, we propose to estimate the background variance of the reconstruction using samples of the micrograph background noise and the distribution of projection directions that occurred in the actual reconstruction (Penczek, 2002b). One possibility would be to calculate a 3-D reconstruction using the windowed noise and in this way obtain a "sample" of a 3-D distribution of noise. However, we estimate other components of the variance in the reconstruction using the bootstrap technique, so we can also apply the same method to the estimation of the background noise, i.e., we can obtain another estimate of σ^2_{Back} by resampling, with replacements, the available projection samples of the background noise. The limitation of using the samples of background noise from micrographs to infer the level of noise in 3-D reconstruction is that the level of noise within the area occupied by the projection of the molecule is reduced by the ratio of the molecule "height" to the ice thickness. The ice thickness is very difficult to measure; moreover, rigorous treatment of the problem would introduce non-linearities into the EM image formation model, as the distribution of noise would depend in the shape of particle. Therefore, we decided to ignore this dependence while keeping in mind that the level of background noise is to some degree overestimated.

The bootstrap procedure comprises the following steps:

1. Select samples of the background noise from the micrograph. Their number has to be the same as the number of available projection images (in the companion paper it is described how to obtain these samples from noise regions of images containing windowed particles).
2. Apply the bootstrap technique described in Section 4.1 to calculate the 3-D variance map of the background noise σ^2_{Back}, which will also contain the reconstruction variance σ^2_{Rec}.
3. Calculate the average level of the background variance $\bar{\sigma}^2_{\text{Back}}$ within the 3-D region corresponding to the support of the structure.

In the last step we assumed that the variance in the reconstruction that is due to the background noise in projection data is uniform, i.e., it does not depend on the location in the 3-D reconstructed volume. This follows from the fact that the noise is uniform in 2-D and the reconstruction algorithm employed is shift-invariant. An additional advantage of using the bootstrap technique for estimation of the background variance is that the result contains also the reconstruction variance. Overall, the result of the procedure is a single number, which specifies the uniform level of error (due to background noise and the reconstruction algorithm) in a 3-D reconstruction of a macromolecule. The test of the bootstrap approach and a comparison with direct estimation based on ergodic principle are included in the Supplementary Material.

Taking advantage of the bootstrap estimate of the background error, the variance of structures should be calculated using the modified version of Eq. (13)

$$\sigma^2_{\text{Struct}} = K\left(\sigma^2_B - \bar{\sigma}^2_{\text{Back}}\right). \tag{14}$$

Note that here we disregarded the variance arising from alignment errors, as there is no method to estimate it independently.

5. Results

In this Section we provide results of tests of the bootstrap technique that help to determine the number of bootstrap volumes required for the estimation of the variance and that demonstrate that the technique works well for both noise-free and noise corrupted date. Additional tests are given in the Supplementary Material.

5.1. Monte-Carlo tests of the bootstrap estimation of the variance

To be able to use the bootstrap technique, we have to know the minimum required size of the bootstrap sample B for the method to yield reliable results. For a set of K projections, the number of possible bootstrap samples is $B = \binom{2K-1}{K-1} \cong 2\exp[2K]$. Obviously, it is impossible to generate all of them; rather, to make calculations manageable, we would like to generate as few as possible. To determine the minimum acceptable number we have to know the convergence properties of the bootstrap estimate of the variance of the sample, or the variance of the variance estimator as a function of both the number of bootstrap samples B and the size of the sample K. Unfortunately, analytical expressions do not exist (Shao and Tu, 1995); instead, we used the Monte-Carlo method to assess the relationship.

We generated K random numbers from a Gaussian distribution $N\left(1, \sigma_\gamma = \sqrt{10}\right)$. These numbers were resampled with replacements B times and for each sample set its average was calculated (this step corresponds to the calculation of a 3-D structure from a resampled set of projections). The

variance σ_B^2 was calculated from this set of B averages (this step corresponds to the calculation of 3-D structure variance). We determined that the variance estimate was underbiased and that, in the case tested, it could be approximated by

$$\frac{K\sigma_B^2}{\hat{\sigma}_\gamma^2} = 1 - \frac{1}{K}, \tag{15}$$

where $\hat{\sigma}_\gamma^2$ is the actual variance of the sample. Thus, the bias is of the order $1/K$ and can be neglected in practice. Next, we similarly confirmed that the variance $\sigma^2_{\sigma_B^2}$ of the resampled variance σ_B^2 does not depend on the sample size K, and is the same as the variance of the estimated variance for a simple normally distributed random sample

$$\sigma^2_{\sigma_B^2} = \frac{2}{B}\hat{\sigma}_\gamma^4. \tag{16}$$

In conclusion, the bootstrap variance estimator is consistent, as its variance vanishes with increased size of the bootstrap sample B, and it is negligibly underbiased. Following Eq. (16), thus the size of the bootstrap sample B depends only on the desired accuracy of the variance estimator to have relative error 0.01 it is sufficient to calculate $B = 200$ bootstrap volumes, which is perfectly manageable.

5.2. Test of the bootstrap estimation of the structure variance in a noise-free case

The tests described in this Section were designed to verify that the bootstrap method yields proper estimates of the structure variance and, on the basis of Eq. (10), the variance of structures. The basic test structure comprised five Gaussian functions: the first one (S) centered with a broad support mimicking the shape of a structure, and the remaining four (A–D) scattered and relatively compact corresponding to "features" of the structure (Fig. 2A)

$$\begin{aligned} f(x,y,z) &= 10\exp\left[0.5\left((x/8)^2 + (y/12)^2 + (z/10)^2\right)\right] \\ &\quad + 3\exp\left[0.5\left(((x-13)/6)^2 + ((y-7)/5)^2 + ((z-11)/4)^2\right)\right] \\ &\quad + 2\exp\left[0.5\left(((x-5)/6)^2 + ((y+5)/8)^2 + ((z+13)/7)^2\right)\right] \\ &\quad - 2\exp\left[0.5\left(((x+11)/9)^2 + ((y+7)/8)^2 + ((z-11)/6)^2\right)\right] \\ &\quad + 1.2\exp\left[0.5\left(((x+13)/6)^2 + ((y-3)/4)^2 \right.\right. \\ &\quad \left.\left. + ((z+5)/5)^2\right)\right] = 10S + 3A + 2B - 2C + 1.2D. \end{aligned} \tag{17}$$

(All parameters are given in voxels.) The size of the volume was 64^3 voxels with $-32 \leqslant x,y,z < 32$. Next, we modified the test structure (Eq. (17)) to randomize features A–D. Both their amplitudes and their shapes were set to vary randomly and we also introduced correlations between some of them (only feature B varied independently) (Figs. 3A and B)

$$\begin{aligned} f(x,y,z) &= 10S + 3A\left(1 + r_1(A/3)^2\right) \\ &\quad + 2B\left(1 + 1.2r_2(B/2)^2\right) \\ &\quad - 2C\left(1 + 2.5(r_1 + r_3)(C/4)^2\right) \\ &\quad + 1.2D\left(1 + (r_1 + 2r_4)(D/1.1)^2\right), \end{aligned} \tag{18}$$

where r_{1-4} are independent Gaussian numbers $N(0,1)$. We generated 1253 quasi-evenly distributed projections of this randomized structure by selecting an independent set of numbers r_{1-4} for each projection direction. In effect, each 2-D image contained a projection of the same basic 3-D shape S, but with different amplitudes of features A–D.

We calculated the structure variance using the bootstrap method with $B = 500$ as the size of the sample (Figs. 3C and D). After generating 500 bootstrap volumes we calculated the 3-D structure variance map σ^2_{SVar}, which we then

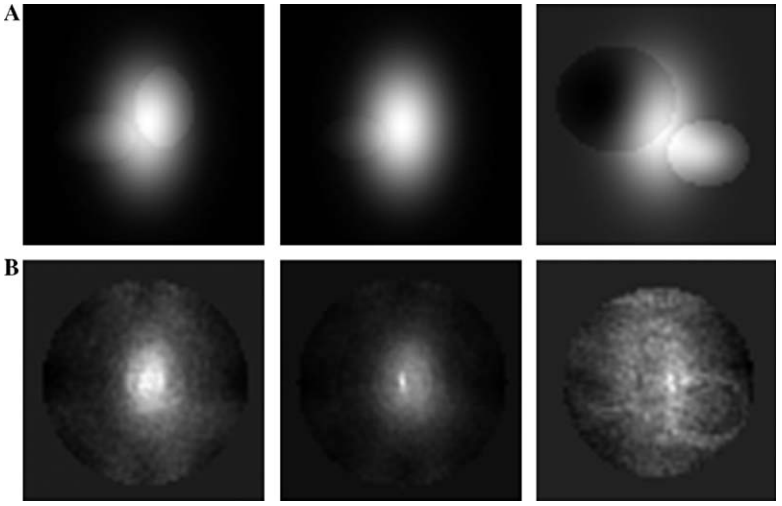

Fig. 2. Test of the variance of the reconstruction estimated using the bootstrap method (see the Supplementary Material). We show selected z-slices ($z = -5$, 0, +11) of the 3-D map masked with a centered sphere with radius $R = 27$ voxels and with the contrast within each slice adjusted independently, so the intensities do not reflect absolute values in respective slices. (A) Model structure (Eq. (17)). (B) Estimated variance.

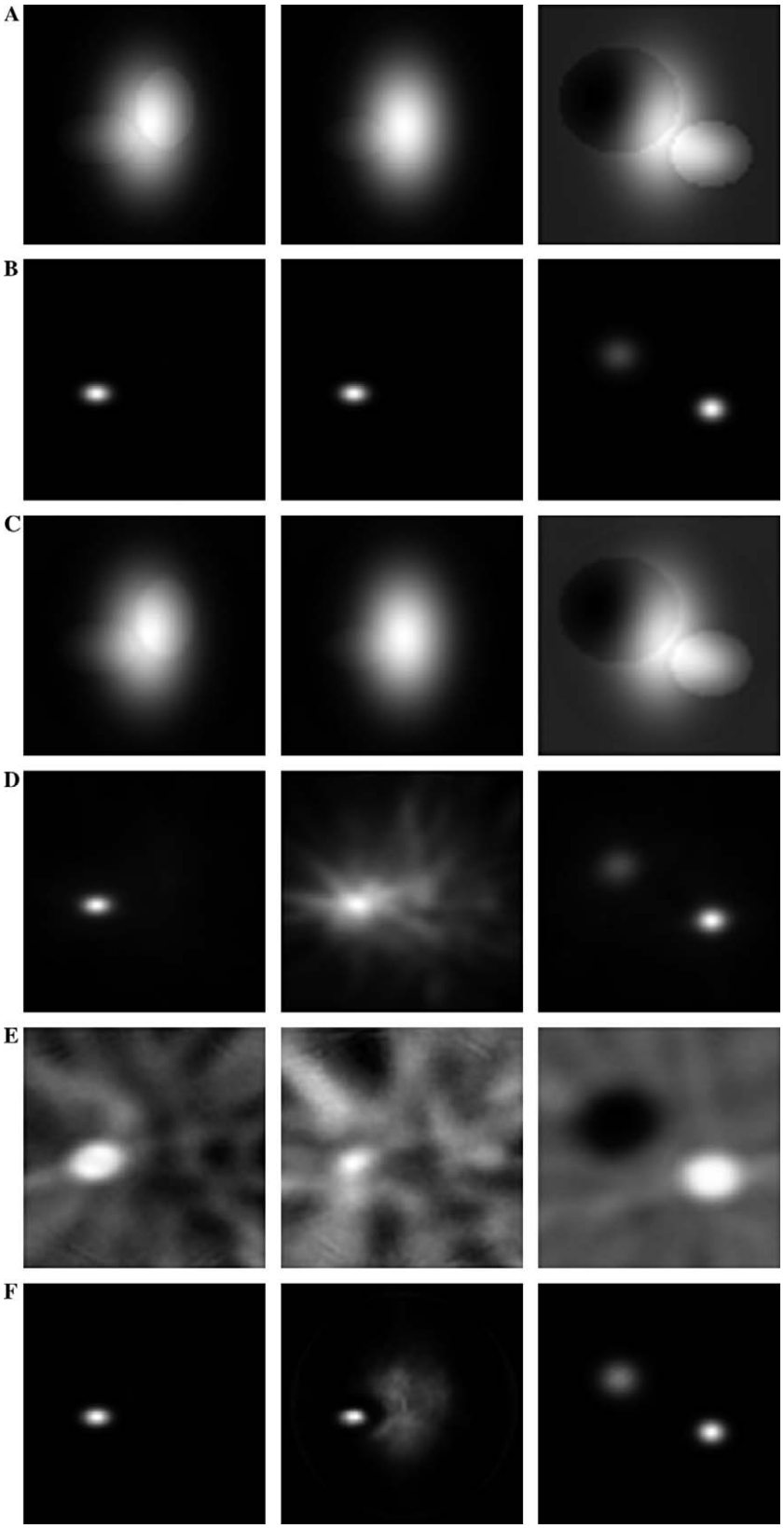

Fig. 3. Test of the estimation of the structure variance in the presence of feature variability using the bootstrap method. We show selected z-slices, left to right: $z = -5$ contains feature D, $z = 0$ with no features, $z = +11$ contains feature A. Contrast within each slice was adjusted independently, so the intensities do not reflect absolute values in respective slices. (A) Average of model structures (Eq. (18)). (B) The variance calculated using 1253 simulated model structures. (C) Average bootstrap structure. (D) Structure variance calculated using the bootstrap method. (E) Correlation map between the center of the feature A and the remaining voxels calculated using sample volumes. (F) Variance calculated using the solvent variance estimation method, i.e., the expectation maximization algorithm described in the Supplementary Material.

multiplied by the number of projections K (=1253) to obtain the 3-D map of variance of structures σ^2_{Struct} (Eq. (10)). The bootstrap variance map (Fig. 3D) corresponds closely to the variance of the test volumes (Fig. 3B). Also, numerical values in bootstrap maps match well values of variance calculated directly using test volumes (Table 1). Since the "features" in the test structure are spread, we decided to compare the average levels of variance within Regions Of Interest (ROIs), which for the purpose of this work we defined as regions around maxima of functions *A–D* that have densities equal to at least 60% of the maximum density of the respective functions. The values of the variances of structures within four ROIs agree very well with the values obtained for the ROIs within the original test volumes. In addition, we calculated the correlation coefficient between the center of the feature *A* and the remaining voxels in the volume (Fig. 3E). The average correlation coefficients (shown in Table 1) within four ROI's agree well with those in the test volume. (The correlation coefficient with the ROI *A* is less than one because it was averaged over the ROI support. The central value is 0.998.) Note that the full correlation function is a four-dimensional entity (64^4) which cannot be easily calculated or displayed.

The variance of structures (Fig. 3D, slice $z = 0$) clearly contains additional components of the variance in comparison with the variance of the test volumes (Fig. 3B). The magnitude of this additional variance can be evaluated based on its values within the central region of the reconstruction (*center* in Table 1), in which we do not expect any variations. We attribute this additional component to the reconstruction variance. It is important to note that the 3-D variance map does not change in a noticeable way even if the size of the bootstrap sample is increased to $B = 5000$ (results not shown).

To put the bootstrap results in a perspective, we calculated the solvent variance using the same test data set and the expectation maximization algorithm described in Supplementary Material. Following this method, correlations in the sources of the variance are ignored; in effect, the relative values of variance within ROIs are distorted.

Table 1
Tests of the bootstrap estimation of the variance of structures

	A	*B*	*C*	*D*	*Center*
σ^2_f	2.25	1.49	0.68	2.37	10^{-8}
σ^2_{Struct}	2.51	1.79	0.93	2.76	0.55
$\sigma^2_{\text{Solvent}}$	15.5	12.2	7.78	17.7	0.77
r_f	1.00	0.02	−0.71	0.48	10^{-7}
r_{Struct}	0.86	0.02	−0.55	0.37	-7×10^{-3}

A–D: ROIs within respective variance/correlation maps. *Center*: ROI defined as a centrally located ball with radius 2 pixels. σ^2_f: variance of test structures. σ^2_{Struct}: variance of structures estimated using the bootstrap technique. $\sigma^2_{\text{Solvent}}$: variance calculated using the method for the solvent variance estimation. r_f, r_{Struct}: correlation coefficients between the central center of the ROI*A* and the centers of all ROIs for the test and bootstrap results, respectively. Correlation coefficients were averaged within respective ROIs.

For example, the upper left peak in the rightmost slice in Fig. 3F has values that are clearly too high. Also, the variance values within the ROIs are entirely incorrect (Table 1). Finally, the method does not yield correlations within the 3-D reconstruction. Despite these inferior results, the method can still be considered useful for a fast estimation of the distribution of the variance within a reconstruction.

5.3. Test of the bootstrap variance estimation method in case of structural variability of the data corrupted by additive uncorrelated noise

In the final test we evaluated the performance of the bootstrap variance estimation method in the case of structural variability of the data corrupted by additive, uncorrelated noise. As the test data set we used the structure designed for testing the structure variance (Eq. (18)) and the set of projections generated for these tests. We corrupted the projections by independent additive Gaussian noise $N(0,30)$, which resulted in $SNR \cong 2$ in the projection data. After generating $B = 500$ bootstrap volumes, we estimated the resolution of an individual reconstruction using the Fourier shell correlation (FSC) (Saxton and Baumeister, 1982) to be 0.1 [1/voxel], applied the corresponding low-pass filtration to all sample volumes, and then calculated the 3-D bootstrap variance map. For a comparison, we applied the same low-pass filtration to the test volumes and calculated their average, variance, and correlation map with respect to the center of feature *A* (Figs. 4A–C). The loss of features in the average map is apparent in Fig. 4A, particularly when compared with the original structure shown in Fig. 2A. The correlation map (Fig. 4C) contains an unusual pattern, which is due to correlations introduced into the volumes by the process of low-pass filtration.

The average of the low-passed bootstrap volumes is shown in Fig. 4D, and the variance in Fig. 4E. The average bootstrap structure is indistinguishable from the average test structure (Fig. 4A) and it is similarly featureless. Nevertheless, despite the high level of noise in the data and severe low-pass filtration of the bootstrap volumes, the structure variance map contains easily distinguishable bright spots in locations corresponding to high level of variance (Fig. 4E, features *D* and *A*). The central slice $z = 0$ of the variance map (Fig. 4E) contains a typical pattern of the featureless background variance. Interestingly, neither the variance nor the correlation maps are inferior to the maps obtained in noise-free case (Figs. 3D and E).

To test the approach given by Eq. (13), we generated projections containing independent additive Gaussian noise $N(0,30)$ and calculated $B = 35$ bootstrap volumes. We applied the same low-pass filtration as used for the volumes containing the structure, calculated the noise bootstrap variance volume, and estimated from it the average background variance $K\bar{\sigma}^2_{\text{Back}} = 0.31$, which we subtracted from $K\sigma^2_{\text{SVar}}$. The values of σ^2_{Struct} obtained are very close to the values calculated for filtered test volumes (Table 2). This demonstrates that the proposed method

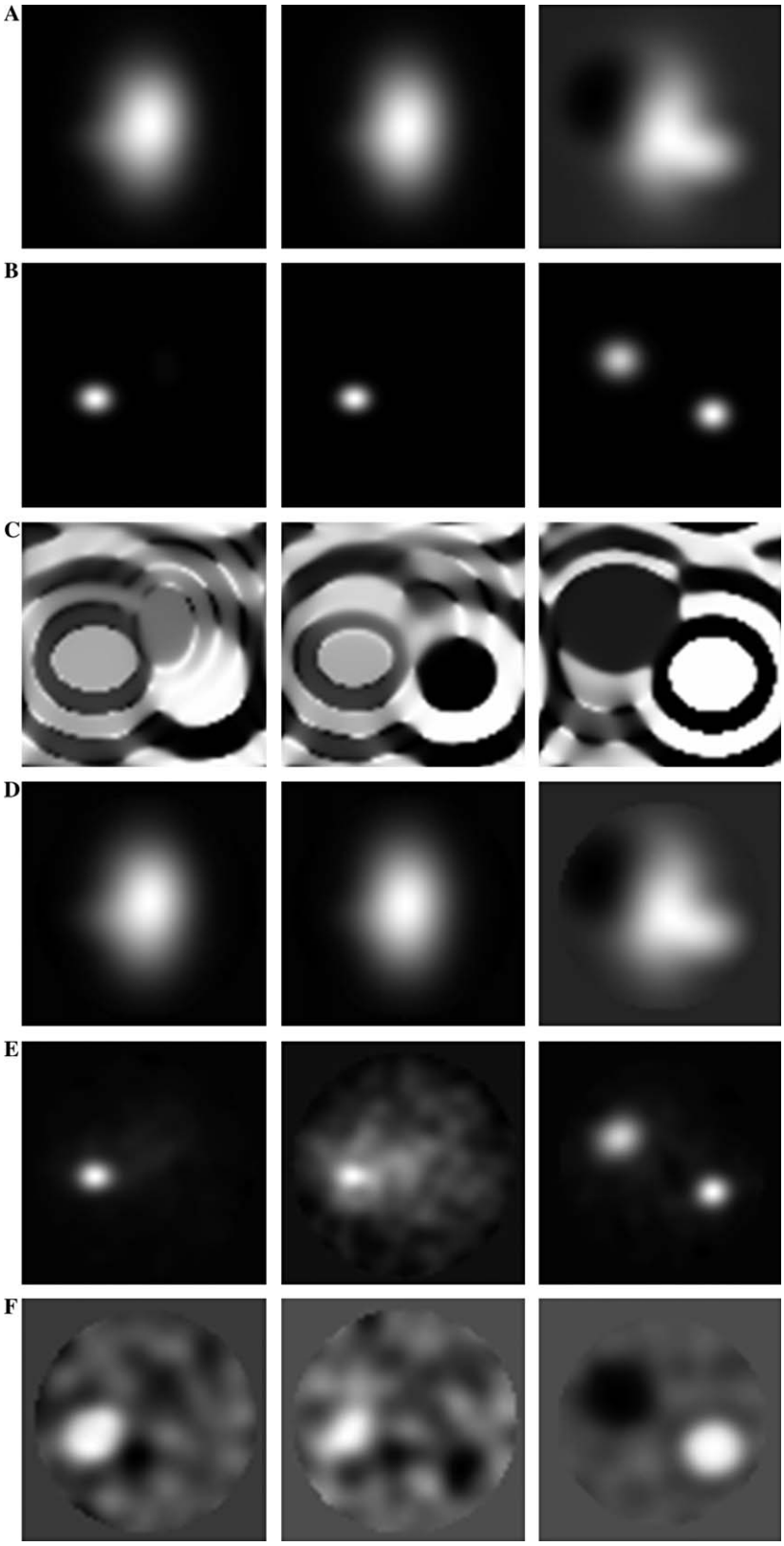

Fig. 4. Test of the estimation of the structure variance using the bootstrap method in the presence of additive independent Gaussian in projections. We show selected z-slices ($z = -5$, 0, +11) with the contrast within each slice adjusted independently, so the intensities do not reflect absolute values in respective slices. (A) Average of low-passed model structures (Eq. (18)). (B) The variance calculated using 1253 simulated low-passed model structures. (C) Correlation map between the center of the feature A and the remaining voxels calculated for simulated low-passed volumes. (D) The average of low-passed bootstrap structures. (E) Structure variance calculated using the bootstrap method and estimated from low-passed sample volumes. (F) Correlation map between the center of the feature A and the remaining voxels calculated using low-passed bootstrap volumes.

Table 2
Test of the estimation of the structure variance using the bootstrap method in the presence of additive independent Gaussian in projections

	A	*B*	*C*	*D*	*Center*
σ_f^2	1.17	1.24	0.65	1.35	4×10^{-2}
$K\sigma_{\mathrm{SVar}}^2$	1.51	1.59	1.14	1.83	0.77
$\sigma_{\mathrm{Struct}}^2$	1.19	1.28	0.82	1.52	0.46
r_f	1.00	0.00	−0.70	0.44	0.19
r_{SVar}	0.87	−0.02	−0.44	0.34	-7×10^{-3}

A–D: ROIs within respective variance/correlation maps. *Center*: ROI defined as a centrally located ball with radius 2 pixels. σ_f^2: variance of test structures. σ_{SVar}^2: structure variance estimated using the bootstrap technique. $\sigma_{\mathrm{Struct}}^2 = K\left(\sigma_{\mathrm{SVar}}^2 - \bar{\sigma}_{\mathrm{Back}}^2\right)$: the variance of structures. $\bar{\sigma}_{\mathrm{Back}}^2$: average background variance estimated using the bootstrap method. r_f, r_{SVar}: correlation coefficients between the central center of the ROI *A* and the centers of all ROIs for the test and bootstrap results, respectively. Correlation coefficients were averaged within respective ROIs.

of calculating the structure variance is sound and that it yields qualitatively correct results.

6. Discussion

We have developed an effective method for the estimation of variance in 3-D reconstructions from projections in single-particle reconstruction. In this method, we take advantage of the large number of individual molecule projections available in single-particle reconstruction and we apply the bootstrap technique to generate multiple sample sets. For each sample set we calculate the sample 3-D reconstruction. The bootstrap variance is finally calculated using a set of sample volumes. In addition, the technique makes it possible to calculate correlations either between voxels in the structure or between regions of interests, usually defined as regions that have high levels of variance. The methods related to the estimation of variance in 3-D reconstructions from projections were implemented in the SPIDER system (Frank et al., 1996) and their comprehensive list is given in Table 3.

The calculation and, in particular, the interpretation of the variance of a structure calculated from a set of projections is intricate due to conceptual and practical difficulties, particularly those caused by the presence of alignment errors. It is expected that projection directions, which are established computationally using an iterative refinement procedure, will have errors. At this point it is not clear whether the variance due to alignment errors can be distinguished from the variance due to structural heterogeneity. As we argued in our earlier paper (Baldwin and Penczek, 2005), there is ambiguity in the possible interpretation of the variance in the data, which can be thought of as caused by alignment errors or the presence of multiple classes of particles in the dataset. To reduce this variance, in the former case one would chose to correct the alignment, while in the latter one would try to classify the data into homogeneous classes. To compound the difficulty, if the structure variance was due to alignment errors it would be problematic to use Eq. (13) and interpret the varience

Table 3
Variance in 3-D structures reconstructed from sets of their 2-D projections

Variance	Notation	Variance model	Estimation method	Command in SPIDER system
Solvent	σ_{Solv}^2	Irregularities of the ice surrounding the particles; radiation/thermal instabilities of macromolecules; it is the variance of the source, ***not*** of the reconstructed map	Expectation maximization 3-D reconstruction algorithm applied to estimates of projection variances	BP EM
Structure variance	σ_{SVar}^2	The variance in the reconstructed 3-D map due to the structure, the reconstruction algorithm, the background, and the alignment errors	Bootstrap applied to 2-D projection data	VA 3Q, VA 3R
Reconstruction	σ_{Rec}^2	The variance in the 3-D map that is due to the reconstruction algorithm and the distribution of projections	Bootstrap applied to 2-D noise-free projection images	VA 3Q, VA 3R
Background	σ_{Back}^2	The variance in the reconstructed map that is due to the background noise in the data	Bootstrap applied to 2-D projection images containing samples of the background noise	VA 3Q, VA 3R
Variance of structures	$\sigma_{\mathrm{Struct}}^2$	The variance of the reconstructed 3-D structure due to conformational variability or ligand binding	Derived from the structure variance	Calculate $K\left(\sigma_{\mathrm{SVar}}^2 - \bar{\sigma}_{\mathrm{Back}}^2\right)$
Covariance (correlation)	r_{ij}	Voxel correlations in the reconstructed map	Calculated from bootstrap volumes of structure variance	VA 3C

K is the number of 2-D projections. In bold we marked three main categories of the variance, as discussed in Section 3.2. $\bar{\sigma}_{\mathrm{Back}}^2$ is the average background variance.

obtained as the variance of structures. Such an interpretation would imply that the reconstructed macromolecules have intrinsically different orientations and that it would therefore be advantageous to cluster them into classes based on their orientations. A more reasonable interpretation is to consider the alignment error as part of the error of the reconstruction, in which case it should not be interpreted in structural terms. Unfortunately, as we already pointed out, we do not have tools as of yet that would allow us to make a distinction between structural and alignment variances.

In the current work, we made a number of simplifying assumptions that allowed us to focus on the analysis on the problem of estimation of variance in reconstructions calculated from sets of their projections. In particular, we ignored the CTF effects. The main reason was that the process of CTF correction itself would constitute another source of variance and at this moment the consensus on how to perform this step computationally has not been reached. In one approach, the particle images are grouped according to associated defocus settings, separate 3-D reconstructions are calculated for each defocus group, and finally merged using a Wiener filtration approach into a single CTF-corrected map (Frank et al., 2000; Penczek et al., 1997). Because of the grouping of the data in this case one would have to modify the resampling strategy accordingly. In another approach, the CTF correction is fused with the 3-D reconstruction process (Grigorieff, 1998; Ludtke et al., 1999), in which case the variance estimation using the bootstrap technique described here could be applied with only minor modifications.

Acknowledgments

We thank Edward H. Egelman, Piotr Franaszczuk, and Anchi Cheng for helpful discussions. Supported by Grants NIH R37 GM 29169 (to J.F.) and R01 GM 60635 (to P.A.P.).

Appendix A. Supplementary material

Supplementary data associated with this article can be found, in the online version, at doi:10.1016/j.jsb.2006.01.003. The SPIDER software in which the variance estimation is implemented is available under an open source agreement at http://www.wadsworth.org/spider_doc/spider/docs/spider.html.

References

Baldwin, P.R., Penczek, P.A., 2005. Estimating alignment errors in sets of 2-D images. J. Struct. Biol. 150, 211–225.

Barrett, H.H., 1990. Objective assessment of image quality: effects of quantum noise and object variability. J. Opt. Soc. Am. A 7, 1266–1278.

Barrett, H.H., Wilson, D.W., Tsui, B.M.W., 1994. Noise properties of the EM algorithm: I. theory. Phys. Med. Biol. 39, 833–846.

Böttcher, B., Wynne, S.A., Crowther, R.A., 1997. Determination of the fold of the core protein of hepatitis B virus by electron cryomicroscopy. Nature 386, 88–91.

Buvat, I., 2002. A non-parametric bootstrap approach for analysing the statistical properties of SPECT and PET images. Phys. Med. Biol. 47, 1761–1775.

Carson, R.E., Yan, Y., Daube-Witherspoon, M.E., Freedman, N., Bacharach, S.L., Herscovitch, P., 1993. An approximation formula for the variance of PET region-of-interest values. IEEE Trans. Med. Imaging 12, 240–250.

Conway, J.F., Cheng, N., Zlotnick, A., Wingfield, P.T., Stahl, S.J., Steven, A.C., 1997. Visualization of a 4-helix bundle in the hepatitis B virus capsid by cryo-electron microscopy. Nature 386, 91–94.

Dahlbom, M., 2002. Estimation of image noise in PET using the bootstrap method. IEEE Trans. Nucl. Sci. 49, 2062–2066.

Davison, A.C., Hinkley, D.V., 1997. Bootstrap Methods and Their Application. Cambridge University Press, New York.

Fessler, J.A., 1996. Mean and variance of implicitly defined biased estimators (such as penalized maximum likelihood): applications to tomography. IEEE Trans. Image Process. 5, 493–506.

Fessler, J.A., Rogers, W.L., 1996. Spatial resolution properties of penalized-likelihood image reconstruction: space-invariant tomographs. IEEE Trans. Image Process. 5, 1346–1358.

Frank, J., 2006. Three-Dimensional Electron Microscopy of Macromolecular Assemblies. Oxford University Press, New York.

Frank, J., Agrawal, R.K., 2000. A ratchet-like inter-subunit reorganization of the ribosome during translocation. Nature 406, 318–322.

Frank, J., Penczek, P., Agrawal, R.K., Grassucci, R.A., Heagle, A.B., 2000. Three-dimensional cryoelectron microscopy of ribosomes. Methods Enzymol. 317, 276–291.

Frank, J., Radermacher, M., Penczek, P., Zhu, J., Li, Y., Ladjadj, M., Leith, A., 1996. SPIDER and WEB: processing and visualization of images in 3D electron microscopy and related fields. J. Struct. Biol. 116, 190–199.

Frank, J., Verschoor, A., Boublik, M., 1981. Computer averaging of electron micrographs of 40S ribosomal subunits. Science 214, 1353–1355.

Gabashvili, I.S., Agrawal, R.K., Spahn, C.M., Grassucci, R.A., Svergun, D.I., Frank, J., Penczek, P., 2000. Solution structure of the *E. coli* 70S ribosome at 11.5 Å resolution. Cell 100, 537–549.

Gao, H., Sengupta, J., Valle, M., Korostelev, A., Eswar, N., Stagg, S.M., Van Roey, P., Agrawal, R.K., Harvey, S.C., Sali, A., Chapman, M.S., Frank, J., 2003. Study of the structural dynamics of the *E. coli* 70S ribosome using real-space refinement. Cell 113, 789–801.

Gao, H.X., Valle, M., Ehrenberg, M., Frank, J., 2004. Dynamics of EF-G interaction with the ribosome explored by classification of a heterogeneous cryo-EM dataset. J. Struct. Biol. 147, 283–290.

Grigorieff, N., 1998. Three-dimensional structure of bovine NADH: ubiquinone oxidoreductase (complex I) at 22 Å in ice. J. Mol. Biol. 277, 1033–1046.

Haley, D.A., Horwitz, J., Stewart, P.L., 1998. The small heat-shock protein, αB-crystallin, has a variable quaternary structure. J. Mol. Biol. 277, 27–35.

Hansen, M.H., Hurwitz, W.N., Madow, W.G., 1953. Sample Survey Methods and Theory. Wiley, New York.

Harauz, G., van Heel, M., 1986. Exact filters for general geometry three dimensional reconstruction. Optik 73, 146–156.

Haynor, D.R., Woods, S.D., 1989. Resampling estimates of precision in emission tomography. IEEE Trans. Med. Imaging 8, 337–343.

Langmore, J.P., Smith, M.F., 1992. Quantitative energy-filtered electron microscopy of biological molecules in ice. Ultramicroscopy 46, 349–373.

Lanzavecchia, S., Bellon, P.L., Radermacher, M., 1999. Fast and accurate three-dimensional reconstruction from projections with random orientations via Radon transforms. J. Struct. Biol. 128, 152–164.

Lanzavecchia, S., Cantele, F., Radermacher, M., Bellon, P.L., 2002. Symmetry embedding in the reconstruction of macromolecular

assemblies via the discrete Radon transform. J. Struct. Biol. 137, 259–272.

Lata, R., Conway, J.F., Cheng, N., Duda, R.L., Hendrix, R.W., Wikoff, W.R., Johnson, J.E., Tsuruta, H., Steven, A.C., 2000. Maturation dynamics of a viral capsid: visualization of transitional intermediate states. Cell 100, 253–263.

Leahy, R.M., Qi, J., 2000. Statistical approaches in quantitative positron emission tomography. Stat. Comput. 10, 147–165.

Liu, W., Frank, J., 1995. Estimation of variance distribution in three-dimensional reconstruction. I. Theory. J. Opt. Soc. Am. A–Opt. Image Sci. 12, 2615–2627.

Ludtke, S.J., Baldwin, P.R., Chiu, W., 1999. EMAN: semiautomated software for high-resolution single-particle reconstructions. J. Struct. Biol. 128, 82–97.

Ludtke, S.J., Jakana, J., Song, J.L., Chuang, D.T., Chiu, W., 2001. A 11.5 Å single particle reconstruction of GroEL using EMAN. J. Mol. Biol. 314, 253–262.

Maitra, R., 1997. Estimating precision in functional images. J. Comput. Graph. Stat. 6, 132–142.

Maitra, R., 1998. An approximate bootstrap technique for variance estimation in parametric images. Med. Image Anal. 2, 379–382.

Maitra, R., O'Sullivan, F., 1998. Variability assessment in positron emission tomography and related generalized deconvolution models. J. Am. Stat. Assoc. 93, 1340–1355.

Marabini, R., Herman, G.T., Carazo, J.M., 1998. 3D reconstruction in electron microscopy using ART with smooth spherically symmetric volume elements (blobs). Ultramicroscopy 72, 53–65.

Palmer, M.R., Bergstrom, M., Beddoes, N.P., Pate, B.D., 1985. Effects of detector wobble motion on image noise in positron emission tomography. IEEE Trans. Med. Imaging MI-4, 58–62.

Penczek, P., 1998. Measures of resolution using Fourier Shell Correlation. J. Mol. Biol. 280, 115–116.

Penczek, P., Radermacher, M., Frank, J., 1992. Three-dimensional reconstruction of single particles embedded in ice. Ultramicroscopy 40, 33–53.

Penczek, P.A., 2002a. Three-dimensional Spectral Signal-to-Noise Ratio for a class of reconstruction algorithms. J. Struct. Biol. 138, 34–46.

Penczek, P.A., 2002b. Variance in three-dimensional reconstructions from projections. Proceedings of the IEEE International Symposium on Biomedical Imaging, Washington, DC.

Penczek, P.A., Grassucci, R.A., Frank, J., 1994. The ribosome at improved resolution: new techniques for merging and orientation refinement in 3D cryo-electron microscopy of biological particles. Ultramicroscopy 53, 251–270.

Penczek, P.A., Renka, R., Schomberg, H., 2004. Gridding-based direct Fourier inversion of the three-dimensional ray transform. J. Opt. Soc. Am. A 21, 499–509.

Penczek, P.A., Zhu, J., Frank, J., 1996. A common-lines based method for determining orientations for N>3 particle projections simultaneously. Ultramicroscopy 63, 205–218.

Penczek, P.A., Zhu, J., Schröder, R., Frank, J., 1997. Three-dimensional reconstruction with contrast transfer function compensation from defocus series. Scan. Microsc. Suppl. 11, 1–10.

Qi, J., Leahy, R.M., 1999. A theoretical study of the contrast recovery and variance of MAP reconstructions from PET data. IEEE Trans. Med. Imaging 18, 293–305.

Qi, J., Leahy, R.M., 2000. Resolution and noise properties of MAP reconstructions in fully 3-D PET. IEEE Trans. Med. Imaging 19, 493–506.

Radermacher, M., 1992. Weighted back-projection methods. In: Frank, J. (Ed.), Electron Tomography. Plenum, New York, pp. 91–115.

Saxton, W.O., Baumeister, W., 1982. The correlation averaging of a regularly arranged bacterial envelope protein. J. Microsc. 127, 127–138.

Shao, J., Tu, D., 1995. The Jackknife and Bootstrap. Springer Verlag, New York.

Spahn, C.M.T., Beckmann, R., Eswar, N., Penczek, P.A., Sali, A., Blobel, G., Frank, J., 2001. Structure of the 80S ribosome from *Saccharomyces cerevisiae*–tRNA–ribosome and subunit–subunit interactions. Cell 107, 373–386.

Unser, M., Trus, B.L., Steven, A.C., 1987. A new resolution criterion based on spectral signal-to-noise ratios. Ultramicroscopy 23, 39–51.

Ushakov, N.G., Ushakova, A.P., 1998. 3D reconstruction from projections for stochastic objects (stochastic tomography). Electronics Letters 34, 512–514.

Valle, M., Zavialov, A., Sengupta, J., Rawat, U., Ehrenberg, M., Frank, J., 2003. Locking and unlocking of ribosomal motions. Cell 114, 123–134.

van Heel, M., Gowen, B., Matadeen, R., Orlova, E.V., Finn, R., Pape, T., Cohen, D., Stark, H., Schmidt, R., Schatz, M., Patwardhan, A., 2000. Single-particle electron cryo-microscopy: towards atomic resolution. Q. Rev. Biophys. 33, 307–369.

Wade, R.H., 1992. A brief look at imaging and contrast transfer. Ultramicroscopy 46, 145–156.

Wilson, D.W., Tsui, B.M.W., 1993. Noise properties of filtered-backprojection and ML-EM reconstructed emission tomographic images. IEEE Trans. Nucl. Sci. 40, 1198–1203.

Zhou, Z.H., Dougherty, M., Jakana, J., He, J., Rixon, F.J., Chiu, W., 2000. Seeing the herpesvirus capsid at 8.5 Å. Science 288, 877–880.

Zhou, Z.H., Liao, W.C., Cheng, R.H., Lawson, J.E., McCarthy, D.B., Reed, L.J., Stoops, J.K., 2001. Direct evidence for the size and conformational variability of the pyruvate dehydrogenase complex revealed by three-dimensional electron microscopy—The "breathing" core and its functional relationship to protein dynamics. J. Biol. Chem. 276, 21704–21713.